Novel strategy to achieve Co_3O_4, CoO and Co_2N hollow nanofibers as advanced anode materials for Li-ion batteries

JIANGDONG GUO, YING YANG, QIANLI MA, XIANGTING DONG*, XINLU WANG, JINXIAN WANG, WENSHENG YU*, GUIXIA LIU, TINGTING WANG
Key Laboratory of Applied Chemistry and Nanotechnology at Universities of Jilin Province, Changchun University of Science and Technology, Changchun 130022, P.R. of China

Co_3O_4 hollow nanofibers were successfully synthesized via a facile electrospinning followed by post-calcination process, CoO and Co_2N hollow nanofibers were respectively obtained via reduction and nitridation of the prepared Co_3O_4 hollow nanofibers in the presence of NH_3 atmosphere at 310 °C and 350 °C. The crystal structure, morphology and compositions of Co_3O_4, CoO and Co_2N hollow nanofibers were investigated by X-ray diffraction (XRD), scanning electron microscopy (SEM), transmission electron microscopy (TEM), energy dispersive spectrometry (EDS). Co_3O_4, CoO and Co_2N hollow nanofibers were explored as the anode materials for Li-ion batteries. Co_3O_4 and CoO hollow nanofibers electrodes have high initial discharge capacity of 883 and 954 $mAh \cdot g^{-1}$, respectively, high coulombic efficiency and stable cycling performance (743 $mAh \cdot g^{-1}$ for Co_3O_4 and 731 $mAh \cdot g^{-1}$ for CoO after 220 cycles) at the current density of 100 $mA \cdot g^{-1}$. Co_2N hollow nanofibers electrode displays outstanding long-term stability (554 $mAh \cdot g^{-1}$ at the 500^{th} cycle with a current density of 100 $mA \cdot g^{-1}$), and excellent rate capability. The superior electrochemical performances are attributed to the unique one-dimensional hollow nanostructure of the materials. The prepared hollow nanofibers are promising anode materials for Li-ion batteries.

(Received May 18, 2017; accepted June 7, 2018)

Keywords: Electrospinning, Reduction, Nitridation, Hollow nanofibers, Li-ion batteries, Long-term stability

1. Introduction

High performance Li-ion batteries (LIBs) for application in electric vehicles (EVs) and hybrid electric vehicles (HEVs) require the development of new electrode materials with good cycling stability, high energy density, and rapid-rate capability. [1, 2] However, currently used commercial graphite anode has low theoretical capacity of 372 $mAh \cdot g^{-1}$, which leads to limited energy output of LIBs. [3] It is still a major challenge to develop new anode materials of high capacity, excellent rate capability and stable cycling performance as an alternative to graphite. In order to meet the above requirements, transition metal oxides, such as Fe_2O_3, [4] Fe_3O_4, [5] NiO, [6] Co_3O_4, [7] CoO, [8] Mn_3O_4, [9] and MnO, [10] have been exploited as anode materials for high performance LIBs because of their high theoretical capacities and the ability to avoid the formation of Li dendrites. Among them, Co_3O_4 and CoO attract extensive interest for LIBs due to their high theoretical capacities (890 $mAh \cdot g^{-1}$ and 715 $mAh \cdot g^{-1}$), which are expected to meet the requirements of future energy storage systems. [11] Metal nitrides are emerging as new and promising electrode materials for electrochemical storage devices such as fuel cell, [12] supercapacitors [13] and high performance LIBs [14] owing to their excellent electrical conductivity, high capacity and their low and flat potentials close to that of lithium metal. [15] Hence, many metal nitrides with high capacity and good stability should be developed as as anode materials for LIBs. Among these metal nitrides, Co_xN holds great promise as anode materials for LIBs since it has significant advantages of high capacity and excellent electrical conductivity. [16] Despite these distinct advantages, the commercial applications of Co_3O_4, CoO and Co_xN anodes in current LIBs are hindered by the rapid capacity fading during cycling, resulting from the large volume expansion upon insertion of Li-ion. [17-19]

In order to improve the Li-storage properties, many researchers have focused on studying nanostructures such as nanospheres, [20] nanowires, [21] nanoplatelets, [22] nanorods, [8] nanosheets, [23] nanocages, [24] nanotubes, [25] nanocubes, [26] and some other more complex ones [27]. The results indicate that the initial discharge capacities increase obviously, and the capacity retention ratios are improved. Among the reported Co_3O_4, CoO and Co_xN nanostructures, one-dimensional (1D) nanomaterials are expected to have high performance in energy storage systems because they have advantages such as large exposed surfaces and short diffusion lengths for Li-ion and direct channels for efficient electron transport, which

enable the materials to interact more efficiently with Li-ion, resulting in high power density. [28] Electrospinning is an outstanding technique to process viscous solutions or melts into continuous fibers with 1D nanostructure, [29] and it is a cheap and simple technique to obtain nanofibers. Electrospinning is widely used to fabricate solid nanofibers and hollow nanofibers. In our early work, we have fabricated $LiFePO_4$/C composite nanofibers and $LiFePO_4$/C/Ag composite hollow nanofibers by electrospinning technology and used the composites as the cathode materials for LIBs. [30, 31] When the hollow-structure nanomaterials are explored as the electrode materials for LIBs, the underlying principle is that the void space within these hollow nanostructures could efficiently enhance their lithium storage properties by shortening the diffusion distance for Li-ion and reversibly accommodating large volume changes. [32] Srinivasan et al. [33] reported that α-Fe_2O_3 hollow nanofibers were prepared by a simple electrospinning technique, which exhibited excellent cycle stability and rate capability. Venugopal et al. [34] reported that Co_3O_4-CNT composites exhibited superior performances with large reversible capacity, good cycling property and rate capability benefiting from the unique hollow and mesoporous Co_3O_4 particle structures. Kim et al. [35] synthesized porous Co_3O_4 hollow rods using bacteria as a soft template, presenting enhanced electrochemical properties. All these works prove that hollow structure is desirable for achieving high capacity and cycling stability of electrode materials. However, it is still a great challenge to fabricate novel and well-defined hollow nanostructures of Co_3O_4, CoO and Co_2N with high lithium storage capacity and excellent cycling stability.

To the best of our knowledge, Co_3O_4, CoO and Co_2N hollow nanofibers for LIBs prepared via effective combination of electrospinning with reduction and nitridation of NH_3 atmosphere have not been reported in the literatures. Herein, we employed electrospinning followed by thermal treatment to fabricate Co_3O_4 hollow nanofibers, and then cleverly used the reduction and nitridation of NH_3 atmosphere for preparation of CoO and Co_2N hollow nanofibers by the control of the calcination temperature, and then they were used as anode materials for LIBs. The morphology, structure and electrochemical performances of the obtained hollow nanofibers were systematically studied. Some new insights into the design and synthesis of electrodes have been proposed, which will be very helpful for the development of future superior performance electrodes.

2. Experimental

2.1. Chemicals

The starting chemical reagents used in this work were as follows. Polyvinyl pyrrolidone (PVP, Mw≈90,000) and *N,N*-dimethylformamide (DMF) were purchased from Tianjin Tiantai Fine Chemical Reagents Co., Ltd. Absolute ethyl alcohol (C_2H_5OH) was bought from Beijing Chemical Plant. Cobalt nitrate hexahydrate ($Co(NO_3)_2 \cdot 6H_2O$) was purchased from Tianjin Fuchen Fine Chemical Factory. Acetylene black, polyvinylidene fluoride (PVDF) and *N*-methyl-*2*-pyrrolidone (NMP) were bought from Sinopharm Chemical Reagent Co., Ltd. All chemicals were of analytical grade and directly used as received without further purification.

2.2. Preparation of Co_3O_4, CoO and Co_2N hollow nanofibers

2.2.1. Preparation of Co_3O_4 hollow nanofibers

Co_3O_4 hollow nanofibers were prepared by calcinating electrospun $Co(NO_3)_2$/PVP composite nanofibers. First, 1.0 g of $Co(NO_3)_2 \cdot 6H_2O$ was dissolved in 10.0 g mixed solvent containing C_2H_5OH and DMF with a mass ratio of 1:1, then 1.0 g of PVP was added into the above solution under magnetically stirring for 10 h to form homogeneous transparent spinning solution. In the spinning solution, the mass ratios of PVP, $Co(NO_3)_2 \cdot 6H_2O$, C_2H_5OH, DMF were 1:1:5:5. Subsequently, $Co(NO_3)_2$/PVP composite nanofibers were prepared by electrospinning technique under a positive high voltage of 14 kV, distance between the capillary tip and the collector was 15 cm, and relative humidity was 40 %-60 %. The collected electrospun composite nanofibers were then calcined at 380 °C in air for 2 h with a heating rate of 1 °C·min^{-1} to obtain Co_3O_4 hollow nanofibers.

2.2.2. Fabrication of CoO and Co_2N hollow nanofibers

Co_3O_4 hollow nanofibers were heated to 310 °C in a quartz boat under a flow of gaseous ammonia with a heating rate of 1 °C·min^{-1} and maintained at that temperature for 6 h, and then calcination temperature was decreased to 100 °C with a cooling rate of 1 °C·min^{-1}, followed by natural cooling down to room temperature, and thus CoO hollow nanofibers were successfully obtained. For preparation of Co_2N hollow nanofibers, the preparative processes were the same as those for CoO hollow nanofibers except that the calcination temperature was 350 °C.

2.3. Characterization methods

Thermogravimetric (TG) and differential scanning calorimetric (DSC) curves were collected by using Pyris Diamond TG-DSC (Perkin Elmer Thermal Analyzer) with the heating rate of 20 °C·min^{-1} in flowing air. The structural characterization of the samples was investigated by an X-ray powder diffractometer (XRD, Bruker, D8FOCUS) in a two-theta range of 10°-90°, and the working voltage and current were kept at 40 kV and 30 mA, respectively. The diameter, morphology and crystal

structure of the samples were analyzed using a field emission scanning electron microscope (FESEM, JSM-7610F, JEOL) and a transmission electron microscope (TEM, Tecnai G2 20 S-Twin, FEI). The elementary compositions of the samples were examined using OXFORD X-MaxN80 energy dispersive spectrometer (EDS) attached to FESEM.

2.4. Electrochemical measurements

The anodes were manufactured using the above obtained nanomaterials as the active materials, acetylene black as conductive additive, and PVDF as binder in the mass ratio of 75:15:10 dissolved in NMP. Then the mixed slurry was coated onto the Cu foil and dried in a vacuum oven at 120 °C for 24 h. Then the film was cut into discs with the loading mass of about 2 $mg \cdot cm^{-2}$. The electrochemical performances of the samples were tested by half cells assembled in an argon-filled glove box (H_2O, O_2 content < 1 ppm). Electrochemical measurements were carried out using 2032-type half cells with a pure lithium foil as the counter electrode, Celgard 2320 as the separator, and 1 $mol \cdot L^{-1}$ $LiPF_6$ in ethylene carbonate/dimethyl carbonate (1:1 v/v) solution as the electrolyte. The charge-discharge performances were performed at room temperature by a battery testing system (BTS-5 V/10 mA, Neware Technology Limited Corporation, China) with a cut-off potential of 0.01 V-3.0 V versus Li^+/Li. Cyclic voltammetry (CV) and electrochemical impedance spectroscopy (EIS) measurements were tested using an electrochemical workstation (CHI-760D, Shanghai Chenhua Instrument Limited Corporation, China). For the CV measurements, the voltage was fixed between 0.01 V and 3.0 V, and the scanning rate was fixed at 0.1 $mV \cdot s^{-1}$. For the EIS measurements, the amplitude of the alternating current signal to the cells was 10 mV and the frequency was between 0.01 Hz and 1 MHz.

3. Results and discussion

3.1. Structure and morphology of Co_3O_4, CoO and Co_2N hollow nanofibers

In order to manifest the decomposition process of $Co(NO_3)_2$/PVP composite nanofibers, TG and DSC analysis were carried out. As illustrated in Fig. 1a, it shows the thermal behavior of $Co(NO_3)_2$/PVP composite nanofibers. The weight loss is involved in three stages in TG curve. The first weight loss is 14.15 % before 99 °C, which is caused by the loss of the surface absorbed water and the dehydration of $Co(NO_3)_2 \cdot 6H_2O$ in the composite nanofibers. The second weight loss is 6.46 % in the range from 99 °C to 247 °C, which is attributed to the loss of the rest of solvent DMF and the decomposition of $Co(NO_3)_2$. The third obvious weight loss (58.17 %) between 247 °C and 275 °C is mainly resulted from the decomposition and combustion of PVP, with an intensive exothermic peak around 272 °C in DSC curve. Above 350 °C, the TG curve is unvaried, the total weight loss is 78.78 %. Therefore, in this study, Co_3O_4 hollow nanofibers were prepared by calcining $Co(NO_3)_2$/PVP composite nanofibers at 380 °C for 2 h.

Crystal structure and phase composition of Co_3O_4 hollow nanafibers were confirmed by XRD measurements. As observed in Fig. 1b, all diffraction peaks are sharp and well-defined, implying that the sample is highly crystallized. It is seen that all the diffraction peaks are indexed as a pure cubic phase of Co_3O_4, which match well with those of the JCPDS standard card (PDF#76-1802, space group *Fd3m*), and no characteristic peaks are observed for other impurities, indicating the high purity of the prepared Co_3O_4.

Typical XRD patterns of the obtained CoO hollow nanifibers are demonstrated in Fig. 1c. All diffraction peaks confirm that the obtained sample can be identified as cubic CoO with space group of *Fm-3m*, in accordance with the JCPDS standard card (PDF#70-2856). Strong and sharp diffraction peaks are situated at 2θ values of 36.52°, 42.42°, 61.55°, 73.74° and 77.61°, corresponding to (111), (200), (220), (311) and (222) crystallographic planes, indicating the formation of pure cubic crystalline CoO.

The XRD patterns of sample obtained via nitriding Co_3O_4 hollow nanofibers at 350 °C are shown in Fig. 1d. All diffraction peaks are well indexed to pure Co_2N (PDF#72-1368, space group *Pmnn*) with orthorhombic structure, where the diffraction peaks are situated at 2θ values of 37.03°, 39.08°, 41.54°, 42.65°, 44.49°, 56.86°, 58.35°, 65.35°, 69.47°, 76.56°, 82.51° and 84.30°, corresponding to (110), (020), (002), (111), (021), (112), (022), (200), (130), (113), (221) and (132) crystallographic planes of the orthorhombic Co_2N, respectively. Notably, no other impurity can be detected, which indicates that the sample has high purity.

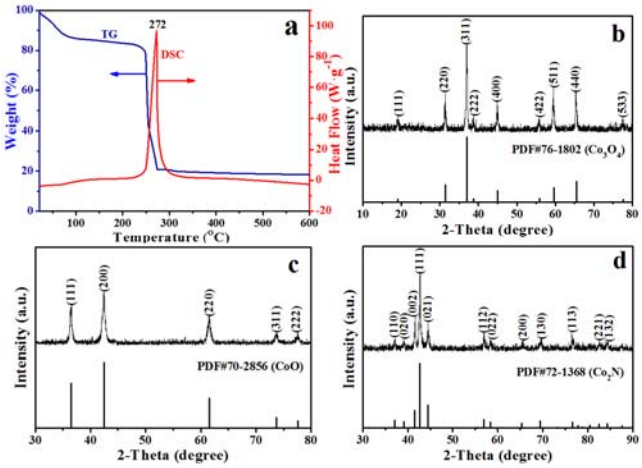

Fig. 1. TG and DSC curves of $Co(NO_3)_2$/PVP composite nanofibers (a); XRD patterns of the obtained Co_3O_4 (b), CoO (c) and Co_2N (d) hollow nanofibers

SEM was employed to investigate the morphologies. Fig. 2a demonstrates the SEM image of $Co(NO_3)_2$/PVP composite nanofibers. It is observed that the fibers have smooth surface. The SEM image of Co_3O_4 hollow nanofibers is shown in Fig. 2b. One can see that the sample retains the morphology of fibers after calcination at 380 °C. The shrink of diameter of Co_3O_4 hollow nanofibers after calcination is due to the decomposition of PVP and inorganic salts. Inset of Fig. 2b illustrates that Co_3O_4 nanofibers possess hollow and well-defined tubular nanostructure. SEM image of the obtained CoO hollow nanofibers reduced at 310 °C is shown in Fig. 2c. After being reduced at 310 °C, the morphology and the structure are similar to those of Co_3O_4 hollow nanofibers. SEM image of the obtained Co_2N hollow nanofibers nitrided at 350 °C is indicated in Fig. 2d. After being nitrided at 350 °C, the nanofibers shrink, but still remain hollow fibrous structure, Co_2N hollow nanofibers have uniform diameter and random orientation. From inset of Fig. 2d, it can be found that the nanofibers are hollow structure, but the inner diameter of hollow nanofibers is reduced.

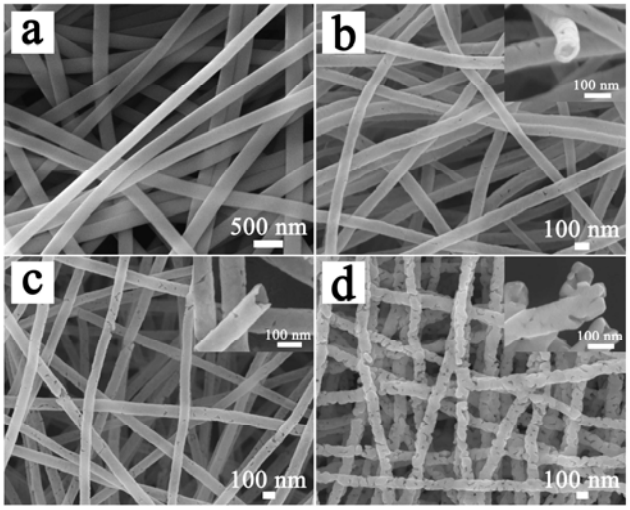

Fig. 2. SEM images of electrospun $Co(NO_3)_2$/PVP composite nanofibers (a), Co_3O_4 hollow nanofibers (b), CoO hollow nanofibers (c) and Co_2N hollow nanofibers (d)

Under the 95 % confidence level, these nanofibers analyzed by Shapiro-Wilk method are normal distribution. Histograms of diameters distribution of the nanostructures are indicated in Fig. 3. The diameters of $Co(NO_3)_2$/PVP composite nanofibers, Co_3O_4 hollow nanofibers, CoO hollow nanofibers and Co_2N hollow nanofibers are 213.14 ± 1.20 nm, 83.09 ± 0.49 nm, 81.17 ± 0.71 nm and 73.99 ± 0.55 nm, respectively.

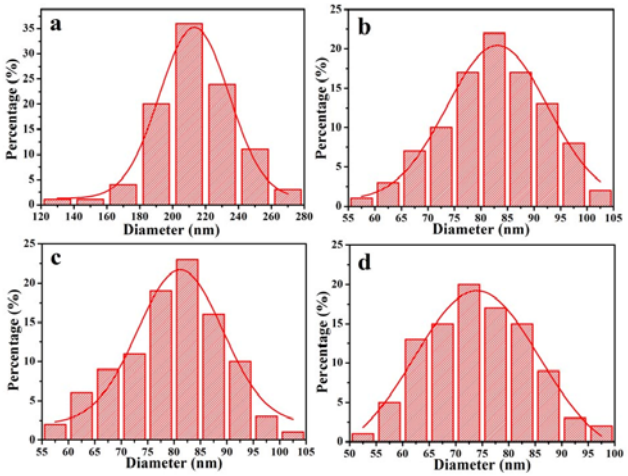

Fig. 3. Histograms of diameters distribution of $Co(NO_3)_2$/PVP composite nanofibers (a), Co_3O_4 hollow nanofibers (b), CoO hollow nanofibers (c) and Co_2N hollow nanofibers (d)

The elementary compositions of $Co(NO_3)_2$/PVP composite nanofibers, Co_3O_4 hollow nanofibers, CoO hollow nanofibers and Co_2N hollow nanofibers were further confirmed by EDS, as revealed in Fig. 4. EDS spectra show that C, N, O, Co are main elements in composite nanofibers, O and Co elements exist in Co_3O_4 and CoO hollow nanofibers. EDS spectrum reveals the presence of Co and N elements in Co_2N hollow nanofibers. The element C, in Co_3O_4, CoO and Co_2N holllow nanofibers, comes from the used conductive tape. The Pt peaks in the spectra come from Pt conductive film plated on the surface of the samples for SEM observation. No other elements are found in the samples, implying that the samples have high purity.

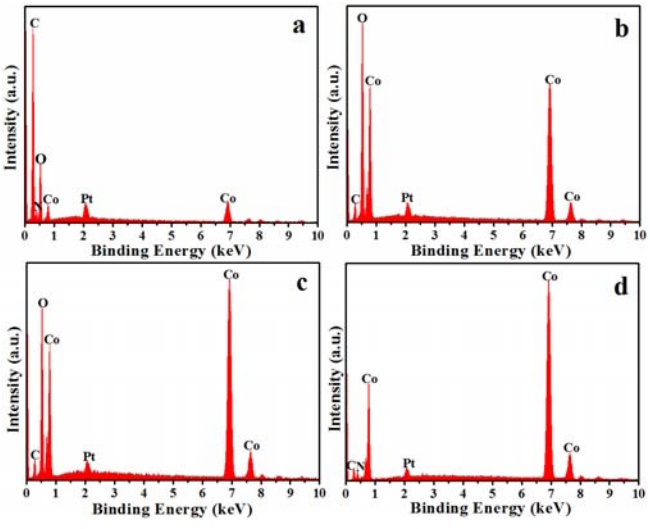

Fig. 4. EDS spectra of $Co(NO_3)_2$/PVP composite nanofibers (a), Co_3O_4 hollow nanofibers (b), CoO hollow nanofibers (c) and Co_2N hollow nanofibers (d)

To provide further insights into the morphology and structure of Co_3O_4, CoO and Co_2N hollow nanofibers, TEM investigations were carried out. Fig. 5a, 5c and 5e show the typical TEM images of Co_3O_4, CoO and Co_2N hollow nanofibers, insets of Fig. 5a, 5c and 5e demonstrate the corresponding selected-area electron diffraction (SAED) patterns. TEM images in Fig. 5a and 5c clearly indicate that Co_3O_4 and CoO nanofibers consist of nanoparticles, and they are hollow structure, which agree with SEM observations. These tiny Co_3O_4 and CoO nanoparticles are densely anchored on the surface of fibers. Inset of Fig. 5a is the SAED pattern of Co_3O_4 hollow nanofibers, it exhibits clear diffraction rings, demonstrating the polycrystalline nature. These ring patterns are assigned to the (220), (311), (511) and (440) reflections of the cubic Co_3O_4 structure (PDF#76-1802), respectively. The SAED pattern (inset in Fig. 5c) corresponding to CoO hollow nanofibers shows a set of diffraction rings, demonstrating the polycrystalline nature, which can be clearly assigned to the diffractions of (111), (200), and (220) crystallographic planes, respectively, of the face-centered cubic structure of CoO (PDF#70-2856). Fig. 5b shows the HRTEM image of Co_3O_4 hollow nanofibers. It is clearly demonstrated the well-textured and crystalline lattice with a distance of 0.47 and 0.29 nm matching very well with the lattice distance of (111) and (220) crystallographic planes of cubic Co_3O_4, respectively. The HRTEM image (Fig. 5d) of CoO hollow nanofibers displays clear crystal lattice with a spacing of 0.25 and 0.21 nm corresponding to the (111) and (200) crystallographic planes, respectively. Fig. 5e shows the TEM image of Co_2N hollow nanofibers, which indicates that the sample is hollow structure and the inner diameter of hollow nanofibers is reduced. The SAED pattern for Co_2N hollow nanofibers is shown in inset of Fig. 5e, which shows highly resolved concentric rings. The diffraction rings indicate the polycrystalline nature of Co_2N hollow nanofibers. The d-values calculated from the rings are: 0.24, 0.21 and 0.12 nm and these correspond to the (hkl) values (110), (111) and (113), respectively. The HRTEM image (Fig. 5f) exhibits clear lattice fringes with spacing of 0.32 and 0.23 nm, which correspond to the (011) and (020) crystallographic planes of orthorhombic Co_2N, respectively.

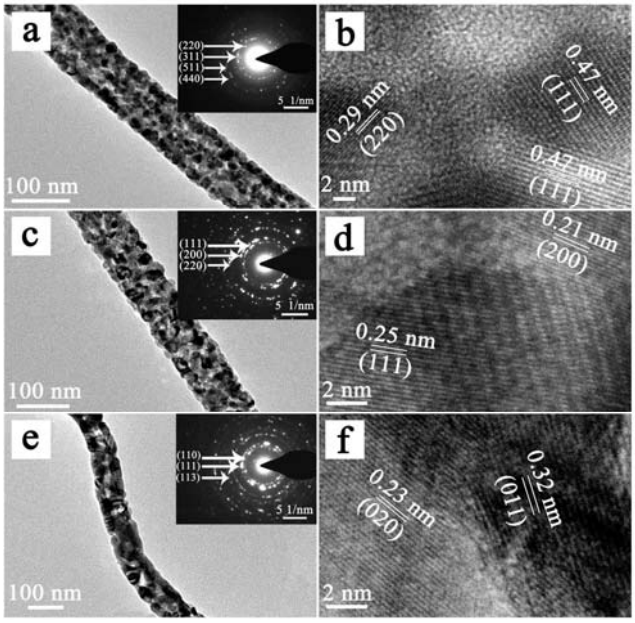

Fig. 5. TEM images (a, c, e) and HRTEM images (b, d, f) of Co_3O_4 (a, b), CoO (c, d) and Co_2N (e, f) hollow nanofibers, the insets of (a, c, e) are the corresponding SAED patterns

Based on the theoretical research and experimental observation, we propose a possible formation mechanism for Co_3O_4, CoO and Co_2N hollow nanofibers, as shown in Fig. 6. Firstly, PVP, residual DMF and $Co(NO_3)_2$ were evenly dispersed in $Co(NO_3)_2$/PVP composite nanofibers after electrospinning (step 1). During calcination process, nitrate was decomposed and formed the Co_3O_4 crystallites, many crystallites were combined into nanoparticles, Co_3O_4 nanoparticles moved to the surface of the composite nanofibers with evaporation of solvent DMF, then some nanoparticles were mutually connected to generate hollow-centered Co_3O_4/PVP composite nanofibers (step 2). As the annealing temperature further increased, PVP was removed from the composite nanofibers via combustion. At the same time, Co_3O_4 located near the surface of the composite nanofibers, and formation of Co_3O_4 hollow nanofibers (step 3). Then, Co_3O_4 hollow nanofibers were heated to 310 °C in a quartz boat under a flow of NH_3

atmosphere, CoO hollow nanofibers were obtained (step 4). When nitridation temperature was 350 °C, Co_3O_4 nanoparticles turned to Co_2N nanoparticles, and Co_2N hollow nanofibers were obtained (step 5).

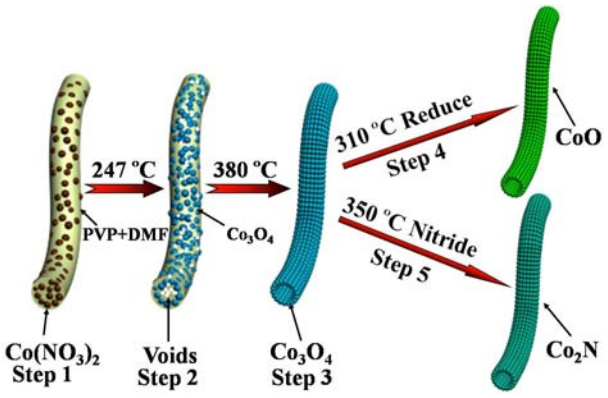

Fig. 6. Possible formation mechanism for Co_3O_4, CoO and Co_2N hollow nanofibers

3.2. Electrochemical performance of Co_3O_4, CoO and Co_2N hollow nanofibers

The discharge and charge profiles of Co_3O_4 hollow nanofibers electrode in the voltage range from 0.01 to 3.00 V (vs. Li^+/Li) at a current density of 100 $mA \cdot g^{-1}$ are shown in Fig. 7a. The plotted data show the 1st, 2nd, 110th, and 220th cycles of discharge and charge. In the first discharge curve, the sample exhibits long voltage plateau followed by a sloping curve down to 0.01 V, the long voltage plateau around 1.18 V is associated with a conversion from Co_3O_4 to an intermediatephase CoO, and then to Co during the lithium insertion process, which is typical of voltage trends for Co_3O_4 electrodes. [29, 36, 37] It is shown that the initial discharge and charge capacities are 883 $mAh \cdot g^{-1}$ and 897 $mAh \cdot g^{-1}$, respectively. The second discharge cycle has a different profile. The voltage plateau originally seen at 1.18 V is no longer observed. Instead, the sloping profile changes at 1.3 V, and then the voltage starts dropping to 0.01 V with a gentle sloping profile, which is also in agreement with the literature. [28, 29, 36, 37] The capacity at the end of the 2nd discharge cycle is 934 $mAh \cdot g^{-1}$ and the charge cycle capacity is about 896 $mAh \cdot g^{-1}$. In the 110th and 220th charge-discharge curves, discharge capacities are 684, 743 $mAh \cdot g^{-1}$ and charge capacities are 677, 730 $mAh \cdot g^{-1}$, respectively, indicating superior cycling stability. The capacity retention over 220 cycles is 84.14 %.

The cycling performance and coulombic efficiency of Co_3O_4 hollow nanofibers electrode at a current density of 100 $mA \cdot g^{-1}$ are shown in Fig. 7b. It is observed that the capacity of 743 $mAh \cdot g^{-1}$ at a current density of 100 $mA \cdot g^{-1}$ is retained after 220 cycles and a good capacity retention is obtained. This is ascribed to the superfine hollow nanofibrous morphology which could enhance the contact between the electrolyte and electrode, facilitate the impregnation of the electrolyte into the electrode, shorten Li-ion diffusion path, the hollow core can buffer against the local volume change during charge-discharge and provide extra space for the storage of Li^+, and hollow nanomaterials have a good contact area and fast diffusion rates along the many grain boundaries existing in them. [33] More interestingly, accompanied with the cycle number increasing, the discharge capacity increases in the initial 15 cycles and then gradually levels off. It is likely that Li-ion diffusion is activated and stabilized gradually during cycling [34]. The coulombic efficiency of every cycle is more than 95.44 %, indicating a high capacity and charge-discharge reversibility of Co_3O_4 hollow nanofibers electrode.

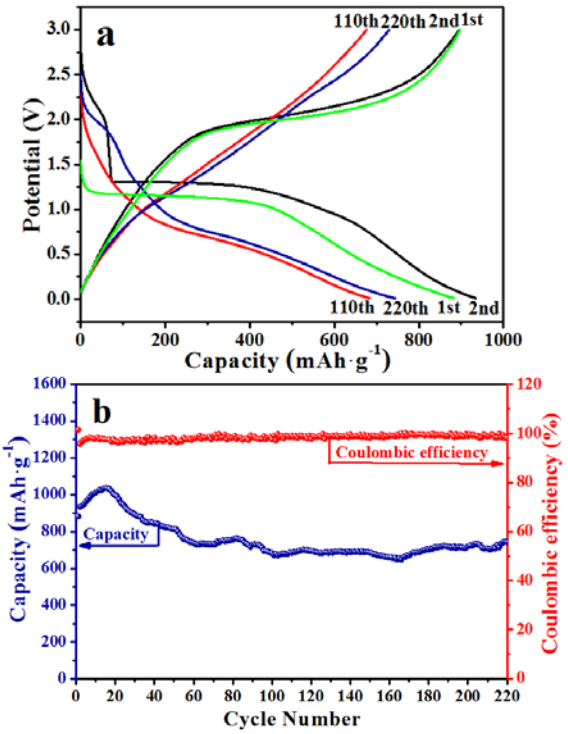

Fig. 7. Discharge and charge profiles (a), cycling performance and coulombic efficiency (b) of Co_3O_4 hollow nanofibers electrode in the voltage range from 0.01 to 3.00 V at a current density of 100 $mA \cdot g^{-1}$

Fig. 8a shows galvanostatic charge-discharge curves of CoO hollow nanofibers electrode in the 1st, 2nd, 110th and 220th cycles at a current density of 100 $mA \cdot g^{-1}$. Similar to the previous report, [38] in the first discharge step, the voltage drops to 1.0 V, subsequently, the profile shows a long voltage plateau at about 0.75 V corresponding to the transformation of CoO to Co, followed by a sloping curve down to the cut-off voltage of 0.01 V. The overall capacity at the end of the first discharge and charge cycles are 954 $mAh \cdot g^{-1}$ and 745 $mAh \cdot g^{-1}$, respectively. There is an irreversible capacity loss of 209 $mAh \cdot g^{-1}$ for the first cycle, which can be mainly attributed to the formation of the solid electrolyte interface (SEI), formation of gel-type polymeric layer and

also partially due to the reduction of the solvent in the electrolyte. [14, 39] For the second discharge step, the discharge plateau voltage increases to 1.6 V, and then drops in a smooth curve till the cut-off at 0.01 V. The total capacities at the end of the second discharge and charge cycles are 763 mAh·g^{-1} and 740 mAh·g^{-1}, respectively. In the 110th and 220th charge-discharge curves, discharge capacities are 564, 731 mAh·g^{-1} and charge capacities are 555, 724 mAh·g^{-1}, respectively, indicating high cycling stability. The capacity retention over 220 cycles is 78.30 %. This trend recurs in the cycle performance test, as shown in Fig. 8b. Fig. 8b shows the cycling performance and coulombic efficiency of CoO hollow nanofibers electrode at a current density of 100 mA·g^{-1}. CoO hollow nanofibers electrode has the first reversible capacity of about 954 mAh·g^{-1}. Accompanied with the cycle number increasing, the discharge capacity increases in the initial 14 cycles and then gradually levels off. It is noted that a high reversible capacity of about 731 mAh·g^{-1} is achieved after 220 cycles, indicating a good capacity retention. Furthermore, after the first cycle, the coulombic efficiency is more than 94.75 %, indicating a high capacity and charge-discharge reversibility of CoO hollow nanofibers electrode.

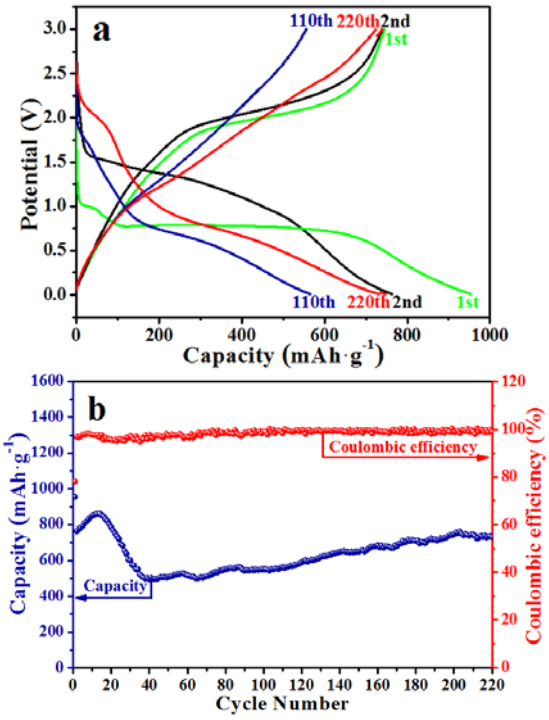

Fig. 8. Discharge and charge profiles (a), cycling performance and coulombic efficiency (b) of CoO hollow nanofibers electrode in the voltage range from 0.01 to 3.00 V at a current density of 100 mA·g^{-1}

The charge-discharge profiles of Co_2N hollow nanofibers electrode at a current density of 100 mA·g^{-1} are shown in Fig. 9a. In the first discharge curve, the discharge curve reveals a voltage plateaus at around 0.25 V, and then drops in a smooth curve till the cut-off at 0.01 V. It is shown that the initial discharge and charge capacities are 201 mAh·g^{-1} and 190 mAh·g^{-1}, respectively, and there is no evident capacity loss. In the 2nd, 250th and 500th charge-discharge curves, discharge capacities are 192, 370, 554 mAh·g^{-1} and charge capacities are 184, 366, 546 mAh·g^{-1}, respectively, indicating high cycling stability. Fig. 9b indicates the coulombic efficiency and cycling performance of Co_2N hollow nanofibers electrode by galvanostatic charge-discharge measurements at a current density of 100 mA·g^{-1}. It is found that the capacity still remains above 554 mAh·g^{-1} after 500 cycles. It is noted that the capacity increases gradually during cycling. For this phenomenon, we propose two possibilities as follows. (i) The decrement of capacity in the initial stage is accompanied with irreversible reactions that generate Co nanoparticles. The metallic particles will increase the overall conductivity of the electrodes. As a result, the charge transfer kinetics will also be improved, resulting in the increment of the capacity in the following cycles. (ii) The decomposition of the electrolyte forms an gel-type polymeric SEI layer on the electrode surface. This SEI layer could improve the mechanical cohesion of the active materials without hindering the ions transfer. The SEI layer could also provide excess lithium ions storage sites by a so-called "pseudocapacitance-type" behavior, especially in the low potential region [40]. The coulombic efficiency of every cycle is more than 94.55 %, indicating a high capacity and charge-discharge reversibility of Co_2N hollow nanofibers electrode.

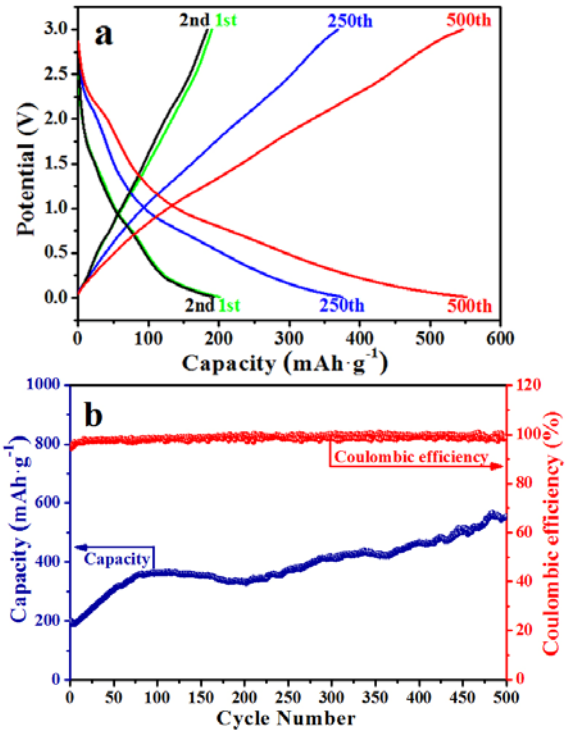

Fig. 9. Discharge and charge profiles (a), cycling performance and coulombic efficiency (b) of Co_2N hollow nanofibers electrode in the voltage range from 0.01 to 3.00 V at a current density of 100 mA·g^{-1}

The electrochemical performances of Co_3O_4 and CoO hollow nanofibers electrodes are compared with Co_3O_4 and CoO-based materials reported in the literatures [11, 27, 39, 41-47] that are summarized in Table 1. The as-prepared Co_3O_4 and CoO hollow nanofibers electrodes show comparable or even better Li storage performance, which could be ascribed to their hollow nanostructure. For the first time, we fabricated Co_2N hollow nanofibers, and further the hollow nanofibers were used anodes for LIBs. To our knowledge, no report on Co_2N used as anode for LIBs is found in the references.

Fig. 10a demonstrates the CV curves of Co_3O_4 hollow nanofibers electrode at a scan rate of 0.1 $mV \cdot s^{-1}$. In the first cathodic scan, there is one intense peak located at around 0.87 V, corresponding to the initial reduction of Co_3O_4 to Co accompanying with the electrochemical formation of amorphous Li_2O, and another weak peak at around 1.12 V, corresponding to the formation of partially irreversible SEI layer. [48] During the subsequent anodic scan, there is a broad peak located at around 2.13 V, which can be ascribed to the oxidation of Co to Co_3O_4 and the decomposition of Li_2O. The lithium storage mechanism of Co_3O_4 electrode can be described by the electrochemical conversion reaction: $Co_3O_4 + 8Li^+ + 8e^- \underset{\text{charge}}{\overset{\text{discharge}}{\rightleftarrows}} 4Li_2O + 3Co$ [2]. From the second cycle, the reduction peak is shifted to a higher potential at about 1.10 V, which is caused by polarization of the electrode material. [49] While the oxidation peak position is almost unchanged. The subsequent CV curves exhibit good reproducibility and similar shapes, suggesting a high reversibility of lithium storage.

The CV curves of CoO hollow nanofibers electrode at a scan rate of 0.1 $mV \cdot s^{-1}$ are shown in Fig. 10b. In the first cycle, the main reduction peak is observed at around 0.63 V, which can arise from the electrochemical reduction reaction of CoO with Li^+, and another weak peak at around 0.92 V, corresponding to the formation of partially irreversible SEI layer. The observed dominant oxidation peak at 2.10 V is ascribed to the oxidation reaction of Co with Li_2O. The lithium storage mechanism of CoO electrode can be described by the electrochemical conversion reaction: $CoO + 2Li^+ + 2e^- \underset{\text{charge}}{\overset{\text{discharge}}{\rightleftarrows}} Li_2O + Co$ [50]. During the subsequent cycles, the main reduction peak is shifted to 1.29 V, peak intensity drops significantly in the second cycle, indicating the occurrence of some irreversible processes in the electrode material in the first cycle. On the other hand, the oxidation peak at around 2.08 V in the anodic sweep exhibits little change in the first three cycles, indicating a good reversibility of the electrochemical reaction.

Fig. 10c manifests the CV curves of Co_2N hollow nanofibers electrode at a scan rate of 0.1 $mV \cdot s^{-1}$. During the first cathodic scan (reaction of Li with Co_2N), the cathodic peaks are observed at around 0.81 V and 1.56 V, these peaks represent the structure-destructure followed by the formation of Co-metal and Li_3N in a two-phase reaction [51]. During the first cathodic scan (Li extraction), the CV shows two peaks at 0.69 V and 2.24 V. These peaks are the indication of decomposition of Li_3N and formation of Co_2N. The subsequent CV curves exhibit good reproducibility and similar shapes, suggesting a high reversibility of lithium storage.

Table 1. Comparison of the electrochemical performances of Co_3O_4 and CoO hollow nanofibers electrodes with existing Co_3O_4 and CoO-based electrodes reported in the literatures

Samples	Current density ($mA \cdot g^{-1}$)	Capacity retention ($mAh \cdot g^{-1}$)/(cycles)	References
Co_3O_4 hollow nanofibers	100	743 (220)	this work
Co_3O_4 mesoporous microdisks	100	765 (30)	41
Co_3O_4 nanoparticles	100	651 (50)	42
Co_3O_4 nanotubes, nanoparticles and nanorods	50	500, 480 and 450 (100)	11
Co_3O_4 powder	120	620 (67)	39
Co_3O_4/C nanowire	100	534 (20)	43
Co_3O_4 hexapods	100	800 (40)	44
CoO hollow nanofibers	100	731 (220)	this work
CoO powder	60	893 (60)	39
Binder-free CoO/graphene	100	640 (150)	27
CoO/C polyhedra	100	510 (50)	45
CoO/C nanocomposites	70	640 (50)	46
CoO hierarchical structure	357	500 (80)	47
Co_2N hollow nanofibers	100	554 (500)	this work

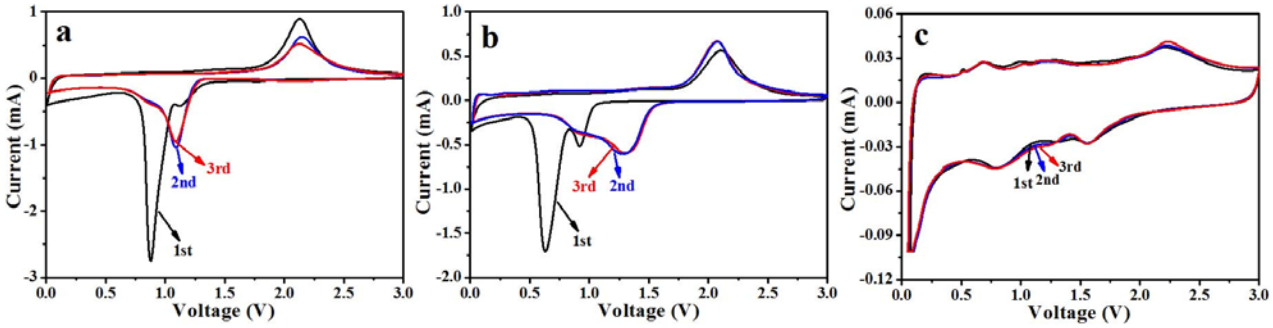

Fig. 10. CV curves of Co_3O_4 (a), CoO (b) and Co_2N (c) hollow nanofibers electrodes

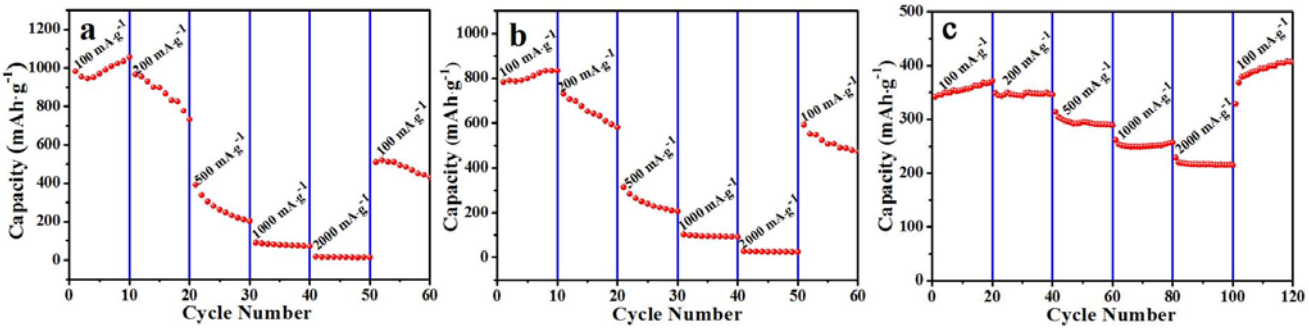

Fig. 11. Rate capability of Co_3O_4 (a), CoO (b) and Co_2N (c) hollow nanofibers electrode at various current densities

In addition, Co_2N hollow nanofibers electrode exhibits much better rate capability compared to Co_3O_4 and CoO hollow nanofibers electrodes operated at various current densities between 100 $mA \cdot g^{-1}$and 2000 $mA \cdot g^{-1}$, as indicated in Fig. 11c, it can be found that the discharge remains stable and decreases regularly with an increased current density. After each 6 cycles at a specific current density, the reversible capacities at 100, 200, 500, 1000 and 2000 $mA \cdot g^{-1}$ are about 371, 346, 289, 257 and 215 $mAh \cdot g^{-1}$, implying that the rate cycling stability of Co_2N hollow nanofibers electrode is excellent. Remarkably, when the current density is again reduced back to 100 $mA \cdot g^{-1}$, the discharge capacity can be recovered (even a little higher than the original capacity at 100 $mA \cdot g^{-1}$) (Fig. 11c). Whereas, the reversible capacities of Co_3O_4 and CoO hollow nanofibers electrodes rapidly drop with an increase current density as indicated in Fig. 11a and 11b.

To further understand the superior electrochemical performances of Co_3O_4, CoO and Co_2N hollow nanofibers electrodes, an EIS measurement was performed with Co_3O_4, CoO and Co_2N hollow nanofibers electrodes. EIS technique is one of the widely used and powerful analytical techniques to investigate charge transfer and Li-ion diffusion kinetics in various electrode materials [52]. Fig. 12 indicates the Nyquist plots in the frequency range from 1 MHz to 0.01 Hz, with the amplitude of 10 mV. All of the measured values have similar Nyquist plots consisting of a semicircle at high frequency region, indicating the charge transfer resistance between the electrode and electrolyte. [53, 54] Apparently, the charge transfer resistance of Co_2N hollow nanofibers electrode is much lower than that of Co_3O_4 and CoO hollow nanofibers electrodes, which can lead to rapid electron transport during the electrochemical lithium insertion/extraction reaction and thus result in significant improvement on the rate performance.

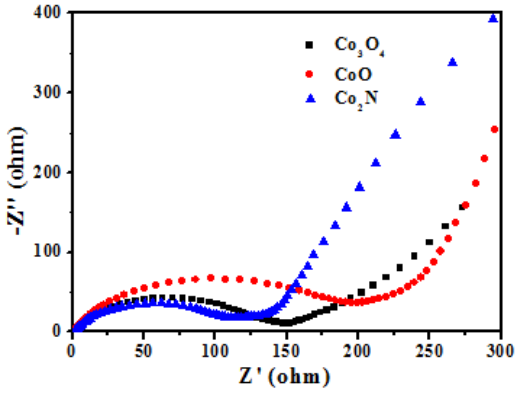

Fig. 12. Nyquist plots of Co_3O_4, CoO and Co_2N hollow nanofibers electrodes

4. Conclusions

In summary, Co_3O_4 hollow nanofibers were successfully synthesized via a facile electrospinning followed by post-calcination process, and then CoO and Co_2N hollow nanofibers were fabricated by reduction and

nitridation of Co_3O_4 hollow nanofibers using NH_3 atmosphere through control of the calcination temperature. The Co_3O_4, CoO and Co_2N hollow nanofibers were used as anode materials for LIBs. Co_3O_4 and CoO hollow nanofibers electrodes demonstrate extraordinary performances, such as high reversible capacity, excellent cycling stability and high coulombic efficiency. Co_2N hollow nanofibers electrode exhibits outstanding long-term stability, high coulombic efficiency and impressive rate capability. The superior electrochemical performances are attributed to the unique 1D hollow nanostructure of the materials. The synthetic method may be extended to the synthesis of other metal oxides and metal nitrides nanostructures as high performance anodes for LIBs.

Acknowledgements

This work was financially supported by National Natural Science Foundation of China (51573023, 50972020, 21601018), Natural Science Foundation of Jilin Province (20170101101JC, 20180520011JH), Industrial Technology Research and Development Project of Jilin Province Development and Reform Commission (2017C052-4), Science and Technology Research Planning Project of the Education Department of Jilin Province during the 13th five-year plan period (JJKH20170608KJ), and Innovative Foundation (XJJLG-2017-04) and Youth Foundation (XQNJJ-2016-01, XQNJJ-2017-17) of Changchun University of Science and Technology.

References

[1] B. Dunn, H. Kamath, J. M. Tarascon, Science **334**, 928 (2011).
[2] G. Y. Huang, S. M. Xu, S. S. Lu, L. Y. Li, H. Y. Sun, ACS Appl. Mater. Interfaces **6**, 7236 (2014).
[3] J. M. Tarascon, M. Armand, Nature **414**, 359 (2001).
[4] J. D. Guo, Y. Yang, W. S. Yu, X. T. Dong, J. X. Wang, G. X. Liu, T. T. Wang, RSC Adv. **6**, 111447 (2016).
[5] E. Kang, Y. S. Jung, A. S. Cavanagh, G. H. Kim, S. M. George, A. C. Dillon, J. K. Kim, J. Lee, Adv. Funct. Mater. **21**, 2430 (2011).
[6] X. H. Wang, X. W. Li, X. L. Sun, F. Li, Q. M. Liu, Q. Wang, D. Y. He, J. Mater. Chem. **21**, 3571 (2011).
[7] X. W. Lou, D. Deng, J. Y. Lee, J. Feng, L. A. Archer, Adv. Mater. **20**, 258 (2008).
[8] F. D. Wu, Y. Wang, J. Mater. Chem. **21**, 6636 (2011).
[9] J. Gao, M. A. Lowe, H. D. Abruña, Chem. Mater. **23**, 3223 (2011).
[10] K. F. Zhong, B. Zhang, S. H. Luo, W. Wen, H. Li, X. J. Huang, L. Q. Chen, J. Power Sources **196**, 6802 (2011).
[11] W. Y. Li, L. N. Xu, J. Chen, Adv. Funct. Mater. **15**, 851 (2005).
[12] Z. H. Wen, S. M. Cui, H. H. Pu, S. Mao, K. H. Yu, X. L. Feng, J. H. Chen, Adv. Mater. **23**, 5445 (2011).
[13] A. Achour, J. B. Ducros, R. L. Porto, M. Boujtita, E. Gautron, L. L. Brizoual, M. A. Djouadi, T. Brousse, Nano Energy **7**, 104 (2014).
[14] P. Yu, L. Wang, F. F. Sun, D. D. Zhao, C. G. Tian, L. Zhao, X. Liu, J. Q. Wang, H. G. Fu, Chem. Eur. J. **21**, 1 (2015).
[15] M. S. Balohun, M. H. Yu, Y. C. Huang, C. Li, P. P. Fang, Y. Liu, X. H. Lu, Y. X. Tong, Nano Energy **11**, 348 (2015).
[16] P. Z. Chen, K. Xu, Y. Tong, X. L. Li, S. Tao, Z. W. Fang, W. S. Chu, X. J. Wu, C. Z. Wu, Inorg. Chem. Front. **3**, 236 (2016).
[17] X. Y. Yao, X. Xin, Y. M. Zhang, J. Wang, Z. P. Liu, X. X. Xu, J. Alloy Compd. **521**, 95 (2012).
[18] H. Guan, X. Wang, H. Q. Li, C. Y. Zhi, T. Y. Zhai, Y. Bando, D. Golberg, Chem. Commun. **48**, 4880 (2012).
[19] B. Das, M. V. Reddy, G. V. Subba Rao, B. V. R. Chowdari, J. Mater. Chem. **22**, 17505 (2012).
[20] J. M. Jeong, B. G. Choi, S. C. Lee, K. G. Lee, S. J. Chang, Y. K. Han, Y. B. Lee, H. U. Lee, S. Kwon, G. Lee, C. S. Lee, Y. S. Huh, Adv. Mater. **19**, 4505 (2013).
[21] K. T. Nam, D. W. Kim, P. J. Yoo, C. Y. Chiang, N. Meethong, P. T. Hammond, Y. M. Chiang, A. M. Belcher, Science **312**, 885 (2006).
[22] Y. Lu, Y. Wang, Y. Q. Zou, Z. Jiao, B. Zhao, Y. Q. He, M. H. Wu, Electrochem. Commun. **12**, 101 (2010).
[23] S. Jiang, R. W. Wang, M. J. Pang, H. B. Wang, S. J. Zeng, X. Z. Yue, L. Ni, S. L. Qiu, Z. T. Zhang, Chem. Eng. J. **280**, 614 (2015).
[24] D. Q. Liu, X. Wang, X. B. Wang, W. Tian, Y. Bando, D. Golberg, Sci. Rep. **3**, 2543 (2013).
[25] J. Xu, L. Gao, J. Y. Cao, W. C. Wang, Z. D. Chen, Electrochim. Acta **56**, 732 (2010).
[26] L. W. Su, Z. Zhou, X. Qin, Q. W. Tang, D. H. Wu, P. W. Shen, Nano Energy **2**, 276 (2013).
[27] X. L. Huang, R. Z. Wang, D. Xu, Z. L. Wang, H. G. Wang, J. J. Xu, Z. Wu, Q. C. Liu, Y. Zhang, X. B. Zhang, Adv. Funct. Mater. **23**, 4345 (2013).
[28] J. S. Cho, Y. J. Hong, Y. C. Kang, ACS Nano **9**, 4026 (2015).
[29] D. Li, Y. N. Xia, Adv. Mater. **16**, 1151 (2004).
[30] D. Q. Shao, J. X. Wang, X. T. Dong, W. S. Yu, G. X. Liu, F. F. Zhang, L. M. Wang, J. Mater. Sci.: Mater Electron. **24**, 4263 (2013).
[31] D. Q. Shao, J. X. Wang, X. T. Dong, W. S. Yu, G. X. Liu, F. F. Zhang, L. M. Wang, J. Mater. Sci.: Mater Electron. **24**, 4718 (2013).
[32] Z. Wang, L. Zhou, X. W. Lou, Adv. Mater. **24**, 1903 (2012).
[33] S. Chaudhari, M. Srinivasan, J. Mater. Chem. **22**, 23049 (2012).
[34] N. Venugopal, D. J. Lee, Y. J. Lee, Y. K. Sun, J. Mater. Chem. A **1**, 13164 (2013).
[35] H. W. Shim, Y. H. Jin, S. D. Seo, S. H. Lee, D. W. Kim, ACS Nano **5**, 443 (2011).
[36] L. Z. Zhuo, Y. Q. Wu, J. Ming, L. Y. Wang, Y. C. Yu,

X. B. Zhang, F. Y. Zhao, J. Mater. Chem. A **1**, 1141 (2013).
[37] R. Tummala, R. K. Guduru, P. S. Mohanty, J. Power Sources **199**, 270 (2012).
[38] J. S. Do, C. H. Weng, J. Power Sources **146**, 482 (2005).
[39] M. V. Reddy, G. Prithvi, K. P. Loh, B. V. R. Chowdari, ACS Appl. Mater. Interfaces **6**, 680 (2014).
[40] J. S. Luo, J. L. Liu, Z. Y. Zeng, C. F. Ng, L. J. Ma, H. Zhang, J. Y. Lin, Z. X. Shen, H. J. Fan, Nano Lett. **13**, 6136 (2013).
[41] Y. H. Jin, L. Wang, J. Gao, J. J. Li, X. M. He, Electrochim. Acta **151**, 109 (2015).
[42] B. Yan, L. Chen, Y. J. Liu, G. X. Zhu, C. G. Wang, H. Zhang, G. Yang, H. T. Ye, A. H. Yuan, Cryst. Eng. Comm. **16**, 10227 (2014).
[43] P. Zhang, Z. P. Guo, Y. D. Huang, D. Z. Jia, H. K. Liu, J. Power Sources **196**, 6987 (2011).
[44] L. M. Wang, B. Liu, S. H. Ran, H. T. Huang, X. F. Wang, B. Liang, D. Chen, G. Z. Shen, J. Mater. Chem. **22**, 23541 (2012).
[45] W. W. Yuan, J. Zhang, D. Xie, Z. M. Dong, Q. M. Su, G. H. Du, Electrochim. Acta **108**, 506 (2013).
[46] S. S. Chu, C. Yang, X. Xia, J. D. Wang, Y. L. Hou, X. T. Su, New J. Chem. **40**, 2722 (2016).
[47] C. C. Chen, Y. N. Huang, H. Zhang, X. F. Wang, Y. J. Wang, L. F. Jiao, H. T. Yuan, J. Power Sources **314**, 66 (2016).
[48] Y. Liu, C. H. Mi, L. H. Su, X. G. Zhang, Electrochim. Acta **53**, 2507 (2008).
[49] D. W. Su, S. X. Dou, G. X. Wang, Nano Res. **7**, 794 (2014).
[50] C. X. Peng, B. D. Chen, Y. Qin, S. H. Yang, C. Z. Li, Y. H. Zuo, S. Y. Liu, J. H. Yang, ACS Nano **6**, 1074 (2012).
[51] B. Das, M. V. Reddy, P. Malar, T. Osipowicz, G. V. Subba Rao, B. V. R. Chowdari, Solid State Ionics **180**, 1061 (2009).
[52] B. G. Choi, S. J. Chang, Y. B. Lee, J. S. Bae, H. J. Kim, Y. S. Huh, Nanoscale **4**, 5924 (2012).
[53] C. N. He, S. Wu, N. Q. Zhao, C. S. Shi, E. Z. Liu, J. J. Li, ACS Nano **7**, 4459 (2013).
[54] M. J. Pang, G. H. Long, S. Jiang, Y. Jia, W. Han, B. Wang, X. L. Liu, Chem. Eng. J. **280**, 377 (2015).

*Corresponding authors: dongxiangting888@163.com;
wenshengyu2009@sina.com